BIOCHEMISTRY
including biophysical chemistry & molecular biology

Article

pubs.acs.org/biochemistry

Localized Permeabilization of *E. coli* Membranes by the Antimicrobial Peptide Cecropin A

Nambirajan Rangarajan,[†] Somenath Bakshi,[†] and James C. Weisshaar*[,†,‡]

[†]Department of Chemistry and [‡]Molecular Biophysics Program, University of Wisconsin—Madison, 1101 University Avenue, Madison, Wisconsin 53706, United States

Supporting Information

ABSTRACT: Fluorescence microscopy enables detailed observation of the effects of the antimicrobial peptide Cecropin A on the outer membrane (OM) and cytoplasmic membrane (CM) of single *E. coli* cells with subsecond time resolution. Fluorescence from periplasmic GFP decays and cell growth halts when the OM is permeabilized. Fluorescence from the DNA stain Sytox Green rises when the CM is permeabilized and the stain enters the cytoplasm. The initial membrane disruptions are localized and stable. Septating cells are attacked earlier than nonseptating cells, and curved membrane surfaces are attacked in preference to cylindrical surfaces. Below a threshold bulk Cecropin A concentration, permeabilization is not observed over 30 min. Above this threshold, we observe a lag time of several minutes between Cecropin A addition and OM permeabilization and ∼30 s between OM and CM permeabilization. The long lag times and the existence of a threshold concentration for permeabilization suggest a nucleation mechanism. However, the roughly linear dependence of mean lag time on bulk peptide concentration is not easily reconciled with a nucleation step involving simultaneous insertion of multiple peptides into the bilayer. Monte Carlo simulations suggest that within seconds, the OM permeability becomes comparable to that of a pore of 100 nm diameter or of numerous small pores distributed over a similarly large area.

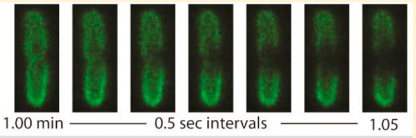

Loss of periplasmic GFP

Antimicrobial peptides (AMPs) are ubiquitous host defense agents essential to the immune system of a variety of organisms, from microbes to insects, plants, and animals.[1] These peptides may prove effective in combating multidrug-resistant pathogens. Literally thousands of AMPs have been discovered in nature, and dozens of synthetic variants have been developed and tested for antibacterial efficacy. They vary in sequence length (up to 50 residues), net charge (often highly cationic), secondary structure (α-helix, β-hairpin), and the fraction, sequence, and composition of hydrophobic and hydrophilic residues.[2,3] The selectivity of attack on bacterial cells vs eukaryotic cells presumably arises from electrostatic attraction of the cationic peptides to the anionic outer layer of both Gram-negative and Gram-positive bacteria. Although it is known that AMPs at sufficiently high concentration disrupt bacterial membranes, the detailed mechanism by which they halt growth and kill bacterial cells is not certain and may well vary from case to case. A clear relationship between peptide sequence and function has not yet emerged. A balance between hydrophobic and hydrophilic residues is important, but amphipathicity is evidently not essential.[2,4] Experiments that mix bulk bacterial cultures with AMPs have revealed information about the timing of antibacterial action as well as biochemical mechanisms.[3] Suggested mechanisms of AMP activity against bacterial cells include interference with cell wall biosynthesis, loss of key periplasmic or cytoplasmic components after permeabilization of membranes, and triggering of signaling pathways that alter the bacterial metabolic state.[2]

There is a long history of biophysical studies of the interaction of AMPs with model lipid bilayers, including large unilamellar vesicles (LUVs) and giant unilamellar vesicles (GUVs).[2] Kinetics studies have monitored the release of LUV content[2,5,6] and the thinning and bursting of GUVs vs time after addition of the AMP.[7−11] In some cases, there is evidence of transient membrane disruption ("graded" content release), whereas in other cases, permeability persists until all content is released ("all or none" release).[12] Structural studies have used X-ray and neutron diffraction,[13] oriented circular dichroism,[14] and NMR[15] to study AMPs bound to multilayers, LUVs, or micelles. Many AMPs fold into amphipathic helices on binding to lipid bilayers.[16] At low surface coverage, helical AMPs bind with the long axis parallel to the membrane surface; the resulting tension leads to membrane thinning.[9] At higher surface coverage, helices insert into the bilayer with the axis perpendicular to the membrane surface.

The nature of the membrane disruptions induced by antimicrobial peptides has been controversial.[2] One standard concept is the formation of discrete pores, either "barrel-stave" or "toroidal". In lipid multilayers, X-ray diffraction provides direct evidence of pore-like structures at high peptide surface density.[13,14] However, recent molecular dynamics simulations argue against a well-defined geometry comprising a fixed number of AMPs.[17,18] Membrane disruptions are likely to be much more disordered and fluxional than depicted by typical cartoons of toroidal pores.[19] A seemingly different concept is the "carpet" model and its variants, all of which involve detergent-like solubilization or micellization of lipids by the

Received: June 18, 2013
Revised: August 26, 2013
Published: August 29, 2013

   dx.doi.org/10.1021/bi400785j | *Biochemistry* 2013, 52, 6584−6594

AMP.[20,21] Carpets could be localized or global. Recent structural studies found a correlation between the activity of antimicrobial oligomers and their ability to form a three-dimensional, inverted hexagonal phase in mixtures with lipids.[22,23] This highly curved phase is perhaps reminiscent of the micelle-like structures proposed in the carpet mechanism. In our view, the distinctions among pores, chaotic pores, localized carpets, and localized "hexagonal phase precursor states" are blurry.

Cecropin A is a well-studied AMP isolated from the moth *Hyalophora cecropia*.[24] Its 37-amino acid sequence contains seven Lys, one Arg, one Glu, and one Asp for a net charge of +7 at neutral pH. (The N-terminus contributes +1, whereas the C-terminus is amidated.) On binding to lipid bilayers, it adopts a helix-break-helix motif, with amphipathic helical segments formed by residues 5−21 and 24−37. At low surface concentrations, both helical segments lie parallel to the lipid bilayer.[25,26] Cecropin A induces content release from lipid vesicles.[27] Both *L* and *D* optical isomers of Cecropin A show comparable ability to kill bacterial cells.[28] Evidently, the killing mechanism is related to interactions with bacterial membranes, not to binding to specific enzymatic targets.

The detailed nature of the membrane disruptions induced by Cecropin A is unclear. Early studies showed that Cecropin A releases encapsulated dye from liposomes and inhibits *E. coli* growth within 10 min of incubation.[29] Cecropin A forms pore-like ion-channels on planar lipid bilayers.[30] In liposomes, Cecropin A disrupts ion gradients at low concentrations, whereas much higher concentrations are required to release encapsulated probes.[31] On the other hand, in bacterial cells, Cecropin A exerts its bactericidal effect, disrupting membrane potential and permeabilizing membranes, at the same concentration.[32] Both "pore-like" and "carpet-like" models have been proposed to explain different experimental results.[21,27] The strength of the connection between studies of model membranes and the mechanisms by which AMPs disrupt real bacterial cell membranes remains to be seen.

Fluorescence microscopy of AMP interactions with single, live bacterial cells provides a completely new level of real-time mechanistic detail that is not discernible from bulk measurements.[33,34] Here, we present a study of the interaction of Cecropin A with single *E. coli* cells in real time with subsecond resolution. Fast movies at 2 frames/s show that the initial OM permeabilization event occurs preferentially in specific membrane regions that depend on whether or not the cell is septating. The event is local and persistent. We directly observe a lag time of several minutes between injection of Cecropin A and disruption of the outer membrane (OM) and a second lag time of ∼30 s between entry of Cecropin A into the periplasm and disruption of the cytoplasmic membrane (CM). Comparisons with Monte Carlo simulations indicate that the initial degree of permeabilization is large and expands over several seconds. Although superficially similar in length, charge, and structure, LL-37 and Cecropin A show different propensities for which membrane locations are attacked and for the degree of permeability induced.

EXPERIMENTAL PROCEDURES

Materials. Cecropin A (Anaspec, catalog no. 24010, > 95% purity) and LL-37 (Anaspec, catalog no. 61302, 95% purity) were purchased as lyophilized powders and used without further purification. All peptide stock solutions were made in sterile, ultrapure (18 MΩ) water. A 5 mM solution (in DMSO) of Sytox Green was purchased from Molecular Probes (S7020). Cell cultures were grown in EZ Rich Defined Medium (EZRDM),[35] which consists of MOPS buffer (M2130, Teknova), nucleic acids (M2103, Teknova), amino acids (M2104, Teknova), glucose (2 mg/mL), K_2HPO_4 (1.32 mM), and NaCl (76 mM).

Bacterial Strains and Cell Cultures. The *E. coli* strain is K12 (MG1655). For experiments monitoring periplasmic GFP, TorA-GFP was expressed from the plasmid pJW1 as previously described.[36] TorA-GFP includes a short sequence (43 residues) from trimethylamine *N*-oxide (TMAO) reductase that signals the twin-arginine translocation (TAT) pathway.[37] The TorA signal sequence is cleaved from GFP in the periplasm. The 12 h MIC of Cecropin A is 0.5 μM.

Cell cultures were grown overnight at 30 °C to stationary phase. Subcultures were grown to exponential phase (optical density ∼0.5 at 600 nm) and injected into the flow chamber for imaging. We selected a region that has at least 10 cells lying flat within the 50 μm diameter observation region prior to initiation of image acquisition and injection of Cecropin A.

Flow Chamber. The flow chamber has been described earlier.[30] It consists of two silicone gaskets (Warner Instruments, catalog no. 64−0335, thickness 375 μm per gasket) sandwiched between two poly-L-lysine-coated glass coverslips (Fisher Scientific). The chamber volume is ∼72 μL. The base plate is maintained at 30 °C by a TC-344B dual channel temperature controller and CC-28 heating cables attached to RH-2 heater blocks (all from Warner Instruments). Solutions are injected into the flow chamber by hand using 1 mL NORM-JECT injection syringes. Typically, ∼400 μL of peptide solution is injected over the course of ∼5 s. By imaging solutions of fluorescent dyes, we have shown that this volume and flow rate fill the chamber uniformly. After injection of the peptide solution, the observation volume remains static throughout the course of the experiment.

Fluorescence Imaging. The flow chamber, microscopy protocol, and the minimum inhibitory concentration (MIC) assay employed in this work have been described earlier.[33] We image Cecropin A-induced permeabilization of the outer membrane to GFP and permeabilization of the cytoplasmic membrane to the DNA stain Sytox Green as follows. The *E. coli* cells export GFP to the periplasm.[36] At $t = 0$, growth medium containing Cecropin A and also 5 nM Sytox Green is injected into the flow chamber over a period of ∼5 s. Sytox Green in buffer is nonfluorescent, but it fluoresces green on binding to chromosomal DNA. On excitation at 488 nm, each single cell exhibits a thin shell of GFP fluorescence. When the outer membrane becomes permeabilized to GFP, the thin shell of fluorescence gradually disappears. In the absence of Cecropin A, we detect no Sytox Green staining of DNA under our conditions. When both the outer membrane and cytoplasmic membrane become permeabilized to Sytox Green, we observe the onset of fluorescence from Sytox Green in a nucleoid staining pattern. To observe localized loss of periplasmic GFP and nucleoid staining by Sytox Green, images are acquired at a frame rate of 2 frames/s with an exposure time of 50 ms/frame.

Cells are typically imaged for 10 min at 2 μM Cecropin A (four times the MIC) and 20 min at 1 μM (twice the MIC). The cost of the peptide precludes studies under flow conditions that would stabilize the bulk concentration. The stated Cecropin A concentrations are only nominal. The actual bulk concentration is likely smaller than that of the injected solution due to unquantified losses at the walls of the flow chamber.

dx.doi.org/10.1021/bi400785j | *Biochemistry* 2013, 52, 6584−6594

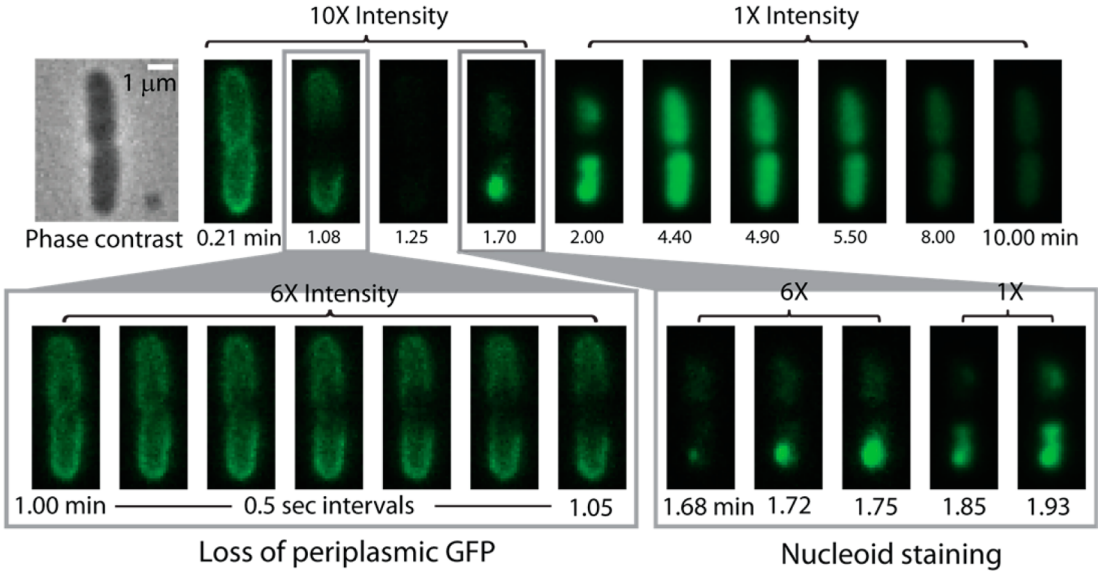

Figure 1. Sequence of events for a septating cell at 2 μM nominal Cecropin A concentration. The overall sequence over 10 min is shown in the top row, whereas expanded views of GFP loss and Sytox Green entry are shown in the bottom row. Note the left−right asymmetry in the loss of GFP from the septal region in the first three frames after t = 1.00 min. Also note punctal entry of Sytox Green into the cytoplasm at t = 1.68 min.

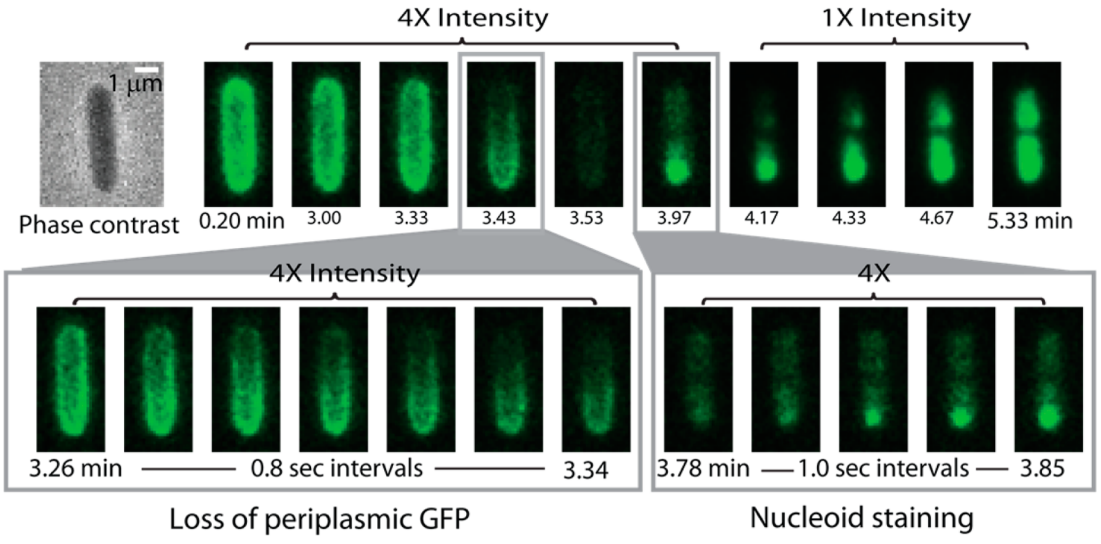

Figure 2. Sequence of events for a nonseptating cell at 2 μM nominal Cecropin A concentration. The overall sequence over 5 min is shown in the top row, and expanded views of GFP loss and Sytox Green entry are shown in the bottom row. Note the loss of GFP from one end-cap (2−4 frames after t = 3.26 min) and predominantly punctal initial staining by Sytox Green.

To monitor cell length vs time (a proxy for growth) in the presence of Cecropin A, the cells are alternately excited by 488 nm and white light at a rate of 1 frame every 3 s with an exposure time of 50 ms/frame. The interleaved fluorescence and white light images are separated during image processing. An elliptical mask is made in MATLAB that matched the cell boundaries. The major axis length of this mask is measured to estimate the cell length vs time for correlation with events in the same cell signaled by changes in fluorescence intensity vs time.

Data Analysis. Images were acquired using Andor Solis (version 4.8.30002.0), and data analyses were performed in ImageJ (version 1.47a), Microcal Origin (version 9.0), and MATLAB (version 7.11.0). To measure the total fluorescence intensity in a single cell, a region of interest (ROI) enclosing the cell was drawn in ImageJ. Background signal was measured by duplicating the same ROI on a region of the image that did not contain a cell. The fluorescence intensity of the ROI corresponding to the cell was measured, and background was subtracted. This process was repeated for each frame of the entire 10−20 min movie. All cells that remain in focus long enough for antimicrobial effects to be observed are included in the analysis. Plots of axial intensity projections are obtained as described in Supporting Information.

RESULTS

Attack on Septating Cells. Late in the cell cycle, as *E. coli* prepares to divide into two daughter cells, the previously straight cylindrical flank of the cell begins to septate at the cell midplane. The parent cell will eventually pinch off two daughter cells, and the septal region will become two new hemispherical end-caps. The early stages of septation are directly observable

dx.doi.org/10.1021/bi400785j | *Biochemistry* 2013, 52, 6584−6594

in phase contrast images and in periplasmic GFP images as a slight depression in the previously straight cell body. In this study, we classify cells as "septating" or "non-septating" on the basis of visual inspection of the phase contrast and periplasmic GFP images; compare Figures 1 and 2. All cells labeled as septating are surely in the process of septation, but some cells in the very early stages of septation will be categorized as nonseptating.

Cecropin A at a nominal concentration of 2 μM, four times the MIC, attacks the membranes of septating cells earlier than nonseptating cells, as described in detail below. The sequence of events in the antimicrobial action of Cecropin A at 2 μM on a septating cell is illustrated in Figure 1. For this particular cell, there is a lag time of ~1 min after injection of Cecropin A during which no effects on GFP are observed. Cecropin A has permeabilized the OM at the nascent septum at t = 1.08 min after addition of the AMP, as shown by the dark septal region due to loss of periplasmic GFP fluorescence. Evidently the loss of periplasmic GFP to the surround is sufficiently rapid that diffusion cannot keep up.

The expanded time scale with images spaced by 0.5 s (Figure 1) shows clearly that the initial loss of GFP causes a *localized* dark patch on one side of the septal region, clear evidence of radially asymmetric loss of GFP. Over 3−5 s, the dark patch spreads around the circumference of the septum, as shown by the images gradually becoming axially symmetric. Over 10−15 s, the dark region spreads axially outward toward the end-caps. The outward flux of GFP is evidently diffusion-limited. About 15 s after the onset of GFP loss (t = 1.25 min), the thin shell of GFP fluorescence has been lost entirely. All septating cells exhibit a central dark patch, but only a few septating cells exhibit the radially asymmetric dark patch. Some localized dark patches may occur near the top or bottom of the cell rather than on the side and thus appear less asymmetric.

For the same cell, after an additional lag time of ~30 s, Cecropin A permeabilizes the CM to Sytox Green, as evidenced by an increase in green fluorescence (t = 1.7 min). The expanded time scale shows that nucleoid staining by Sytox Green begins near one end-cap as a bright dot, indicating *localized* entry into the cytoplasm. Evidently, binding to DNA is sufficiently strong that the earliest Sytox Green molecules diffuse only a short distance within the nucleoid region before binding. Subsequent entry and binding of more Sytox Green causes the bright initial dot to spread. In this particular cell, the staining pattern suggests that a second localized disruption of the CM occurs in the other half of the cell beginning at t = 1.85 min. In many cases, only one bright dot is observed.

Attack on Nonseptating Cells. When Cecropin A at nominal concentration of 2 μM attacks nonseptating cells, permeabilization of the OM and loss of periplasmic GFP almost always begin near one end-cap. The lag time is 2−8 min, much longer than that for septating cells. As illustrated in Figure 2, periplasmic GFP is lost from one end of the cell. For this particular cell, OM permeabilization occurs almost 4 min after injection of Cecropin A. The dark patch spreads across the entire cell periphery in ~15 s, as shown in the expanded view. In five examples, the nonseptating cell under study had remained adhered to its sister cell prior to the Cecropin A attack, enabling us to distinguish the new pole from the old pole. The OM permeabilization always occurs at the new pole.

The subsequent permeabilization of the CM to Sytox Green occurs 32 s after the OM is permeabilized to GFP. CM permeabilization is again fairly localized in space, as evidenced by an initial bright dot of fluorescence that gradually spreads across both nucleoid lobes. The location of CM permeabilization varies from cell to cell, as described next.

Distribution of Permeabilization Events Along the Cell Axis. In Figure 3, the axial locations of each pair of OM and CM permeabilization events are plotted using a relative axial coordinate scale. Here, x_{rel} = 0 is defined as one tip of the cell, and x_{rel} = 1 is defined as the other tip. The septum lies near x_{rel} = 0.5. In septating cells, x_{rel} = 0 is chosen arbitrarily at one tip. In nonseptating cells, x_{rel} = 0 is defined as the tip near which GFP loss begins. Details regarding cell coordinates and determination of the values of x_{rel} at which GFP leaves and Sytox Green enters are given in Supporting Information (Figure S2).

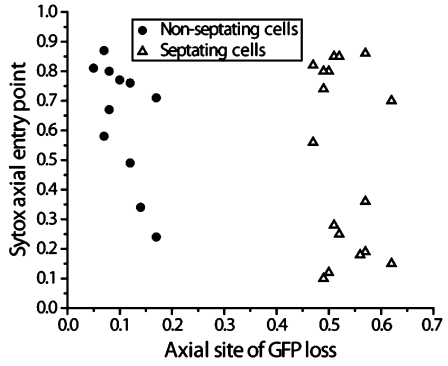

Figure 3. Correlation of axial locations of GFP loss vs Sytox Green entry, with axial location defined on a relative scale from 0 to 1 (tip-to-tip). For nonseptating cells (circles), 0 is chosen at the end of the cell from which GFP leaves. Sytox Green tends to enter the cytoplasm at locations distant from the GFP exit point. For septating cells (triangles), choice of 0 is arbitrary. GFP leaves near the septum, whereas Sytox Green enters near one pole. See Supporting Information for details of measurements.

In visibly septating cells, GFP is always lost from the septal region, whereas Sytox Green tends to enter the cytoplasm near one end-cap. This occurs in spite of the fact that the concentration of Cecropin A within the periplasm must initially be highest near the septum, where entry into the periplasm occurs. For nonseptating cells, permeabilization of the OM to GFP occurs preferentially near one end-cap (x_{rel} ~ 0.1). The subsequent site for permeabilization of the CM to Sytox Green is broadly distributed along the cell axis but tends to occur on the half of the cell distal to the OM permeabilization site. There is a preference for the opposite end-cap.

Timing of Membrane Permeabilization Events and Cell Shrinkage Events vs Cecropin A Concentration. We have also measured the distribution of timings of specific membrane permeabilization events across cells and correlated these events with the halting of cell growth. An example of total green fluorescence intensity vs time for a single, nonseptating cell, obtained at an acquisition rate of 1 frame every 6 s and corrected for background intensity, is shown in Figure 4 (green trace). We define t = 0 as the time of injection of Cecropin A at nominal 2 μM concentration. As evidenced by the transverse intensity linescan (Supporting Information Figure S1), the green fluorescence intensity prior to addition of Cecropin A is due primarily to periplasmic GFP, with small contributions from cytoplasmic autofluorescence and from GFP that has not been exported to the periplasm. At t_{OM} = 4.8 min, the outer membrane is permeabilized to GFP and the cell length shrinks.

dx.doi.org/10.1021/bi400785j | *Biochemistry* 2013, 52, 6584−6594

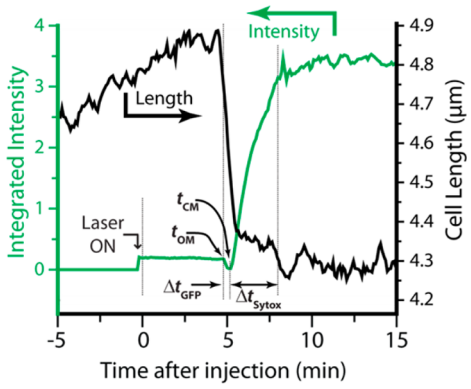

Figure 4. Plot of green fluorescence intensity (green) and cell length (black) vs time for one nonseptating cell at nominal Cecropin A concentration of 2 μM. The laser is turned on just prior to Cecropin A injection at $t = 0$. Lag times to onset of GFP loss from periplasm (t_{OM}) and to Sytox Green entry into cytoplasm (t_{CM}) are shown. Time intervals required for loss of GFP from periplasm (Δt_{GFP}) and entry of Sytox Green into cytoplasm (Δt_{Sytox}) are also indicated.

The cell loses all fluorescence intensity over the next 18 s. At t_{CM} = 5.2 min, the CM is permeabilized to Sytox Green and the fluorescence abruptly rises, this time in a nucleoid-staining pattern. The Sytox Green signal plateaus when all binding sites are saturated and then slowly decreases due to photobleaching. Analogous measurements were carried out for Cecropin A at nominal concentrations of 1 and 4 μM (twice and eight times the MIC). Data from multiple experiments (four experiments at 1 μM, seven at 2 μM, and one at 4 μM, with each experiment involving 5−15 unique cells) was pooled to obtain cell-averaged results.

In Figure 5A, we compare histograms of t_{OM} for septating and nonseptating cells at 2 μM Cecropin A. The mean value $\langle t_{OM} \rangle$ is 100 ± 39 s (±one standard deviation) for septating cells, compared with 225 ± 94 s for nonseptating cells. Both distributions are broad, with standard deviations about half the mean. This ensemble data clearly indicates that the membranes of septating cells are permeabilized earlier than those of nonseptating cells, as in the examples of Figures 1 and 2.

The bulk Cecropin A concentration significantly affects the distribution of t_{OM}. In Figure 5B, we compare 1 and 2 μM in histograms including all cells, both septating and nonseptating. At 1 μM, the distribution has a long tail. As the nominal concentration increases from 1 to 2 to 4 μM, the mean value $\langle t_{OM} \rangle$ for all cells combined decreases from 540 ± 300 to 183 ± 99 to 108 ± 51 s. In Figure 5C, we show a histogram of the lag time between OM permeabilization and CM permeabilization, $(t_{CM} - t_{OM})$, at 1 and 2 μM bulk Cecropin A. The two histograms are similar, except for several outliers at long delay times for the 1 μM data. The breadth of the distribution of t_{OM} is quite similar to that of t_{CM} (Supporting Information Figures S3, S4, and S5), whereas the breadth of the distribution of $(t_{CM} - t_{OM})$ is much smaller. Most of the variability in t_{CM} is due to variability in t_{OM}.

Table 1 summarizes $\langle t_{OM} \rangle$, $\langle t_{CM} \rangle$, and $\langle t_{CM} - t_{OM} \rangle$ for septating, nonseptating, and all cells combined at all three Cecropin A concentrations. Additional histograms partitioning the data into septating and nonseptating cells are included as Supporting Information Figures S3 and S4.

Finally, we measured cell length vs time from the interspersed phase contrast images, enabling us to correlate the apparent halting of cell growth with the membrane

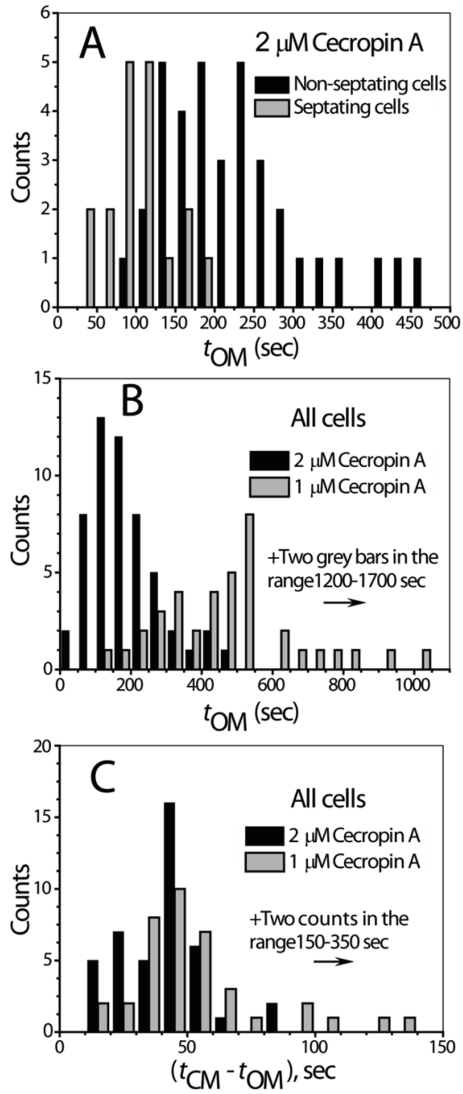

Figure 5. Histograms of timing events for onset of permeabilization of outer and cytoplasmic membranes. (A) Comparison of the distribution of t_{OM} for septating vs nonseptating cells at nominal 2 μM Cecropin A. (B) Comparison of the distribution of t_{OM} for all cells at nominal 1 vs 2 μM Cecropin A. (C) Comparison of the distribution of $(t_{CM} - t_{OM})$ for all cells at nominal 1 μM vs 2 μM Cecropin A. Bin width is 25 s in panel A, 50 s in panel B, and 10 s in panel C.

permeabilization events. An example for a septating cell at 2 μM Cecropin A is included in Figure 4 (black trace). Prior to injection of Cecropin A, cell length gradually increases with time. Cell growth halts abruptly at t = 4.7 min, some 6 s before the onset of GFP loss, and the cell gradually shrinks in length by 12% over the next 40 s. This is the general pattern for both septating and nonseptating cells at all three concentrations studied. After shrinkage, cell length levels off and does not recover. Significantly, permeabilization of the CM to Sytox Green (and presumably the loss of the transmembrane potential) consistently occurs about 30 s *later* than the start of cell shrinkage. We suggest that the abrupt shrinkage is an osmotic effect that occurs at the same time as entry of Cecropin A into the periplasm, but the detailed mechanism is unclear. Similar shrinkage events were observed for LL-37 on *E. coli* and on *B. subtilis* in earlier work.[33,34]

There is mild evidence that Cecropin A at 2 μM sometimes decreases the cell growth rate shortly after injection and well

dx.doi.org/10.1021/bi400785j | *Biochemistry* 2013, 52, 6584−6594

Table 1. Summary of mean timing data for OM and CM permeabilization of *E. coli* by Cecropin A.[a]

	nominal bulk Cecropin A concentration		
	1 μM	2 μM	4 μM
N_{tot} (all cells)	43	54	7
$\langle t_{OM} \rangle$	540 ± 300	183 ± 99	108 ± 51
$\langle t_{CM} \rangle$	601 ± 310	222 ± 97	129 ± 49
$\langle t_{CM} - t_{OM} \rangle$	64 ± 53	39 ± 17	21 ± 9
$\langle \Delta t_{GFP} \rangle$	22 ± 21 (N = 36)	15 ± 10 (N = 52)	15 ± 6
$\langle \Delta t_{Sytox} \rangle$	98 ± 47	92 ± 44	117 ± 47
N_{sept} (septating)	13	18	3
$\langle t_{OM} \rangle$	350 ± 120	100 ± 39	62 ± 9
$\langle t_{CM} \rangle$	410 ± 140	147 ± 45	84 ± 6
$\langle t_{CM} - t_{OM} \rangle$	63 ± 39	47 ± 14	22 ± 9
$\langle \Delta t_{GFP} \rangle$	23 ± 12 (N = 12)	17 ± 8	18 ± 6
$\langle \Delta t_{Sytox} \rangle$	85 ± 31	71 ± 23	78 ± 12
$N_{nonsept}$ (nonseptating)	30	36	4
$\langle t_{OM} \rangle$	620 ± 320	225 ± 94	143 ± 38
$\langle t_{CM} \rangle$	680 ± 330	259 ± 95	164 ± 34
$\langle t_{CM} - t_{OM} \rangle$	65 ± 59	34 ± 17	21 ± 9
$\langle \Delta t_{GFP} \rangle$	22 ± 25 (N = 24)	14 ± 11 (N = 34)	15 ± 6
$\langle \Delta t_{Sytox} \rangle$	104 ± 52 (N = 29)	103 ± 49	117 ± 47

[a]All times are in seconds. The ± values are one standard deviation of single measurements. N values give the number of cells in the calculation of each mean.

before the OM permeabilization event. In Supporting Information Figure S6, the plot of length vs time is curving upward prior to injection of Cecropin A, but the curvature decreases immediately after injection. This decrease in the *rate* of growth is evident in 4 of the 6 cases examined closely. Perhaps a stress signal transmitted through both membranes has slowed growth before Cecropin A permeabilizes the OM.[38] Alternatively, some Cecropin A molecules may translocate across the OM and effect cell wall growth prior to forming GFP-sized disruptions. A similar slowing of growth of *B. subtilis* was observed on injection of sublethal concentrations of LL-37.[34]

Time Scale of GFP Release and of Sytox Green Entry. We can infer something of the nature and magnitude of the membrane disruption from the time course of the release of GFP from the periplasm (Δt_{GFP}, Figure 4) and the entry of Sytox Green into the cytoplasm (Δt_{Sytox}). Because each curve may have a different shape, we define Δt_{GFP} as the time required for the GFP signal to decay from 90% to 10% of its initial value and Δt_{Sytox} as the time required for the Sytox Green signal to rise from 10% to 90% of its final value. Histograms of the distribution of these values are given in Supporting Information Figures S3, S4, and S5. Means and standard deviations are provided in Table 1 for the three Cecropin A concentrations studied. The values of Δt_{GFP} will constrain Monte Carlo simulations of GFP loss, as described below.

The rate of release of GFP shows distinct behavior for different cells, as shown in Figure 6 for two septating cells at 2 μM Cecropin A. In most cells, the GFP loss is quite abrupt, but in a few cells, the loss is initially gradual. The more gradual release events seem somewhat more likely for septating cells (4 out of 13 examples) than for nonseptating cells (2 out of 15). In cells that exhibit the more gradual GFP loss, the dark patch occurs first on one-half of the cell, but it is more delocalized and less sharply delineated at early times. The slower the GFP

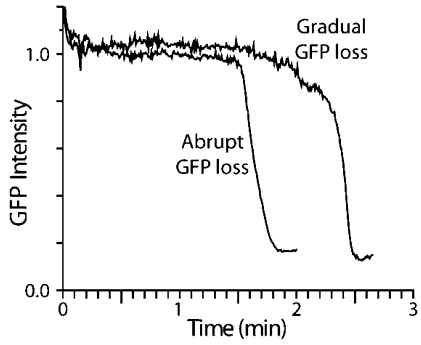

Figure 6. Expanded view of loss of periplasmic GFP for two cells, both septating, at nominal Cecropin A concentration of 2 μM. Most cells exhibit the abrupt loss behavior; see text.

loss, the more effectively diffusion competes with efflux. The Monte Carlo simulations described next provide quantitative insights into the magnitude of membrane permeability and how it changes over time after the initial disruption event.

Simulations of GFP Loss from the Periplasmic Space. The spatial and temporal course of GFP release from the periplasm is governed by the diffusion coefficient of GFP and the size, location, and permeability of the OM disruption. We have carried out Monte Carlo (random walk) simulations of diffusion to an absorbing patch on the outer membrane in a model geometry chosen to mimic the periplasm: a thin space between two nested spherocylinders (Figure 7A). The GFP population is modeled as 20 000 point particles, initially randomly distributed in the periplasmic space. The permeable region of the outer membrane is modeled as a perfectly absorbing patch.[39] A particle is removed from the simulation whenever it crosses the absorbing surface patch. No "re-crossings" of the surface patch are permitted, meaning that the model yields the fastest possible leakage of GFP through a hole in the OM. In comparison, both a pore of finite thickness and a carpet patch would transmit GFP less efficiently. Parameters of the simulation include the GFP diffusion coefficient D_{peri}, the periplasm thickness d, and the geometry and location of the absorbing patch. Details are given in Supporting Information.

For septating cells, we experimented with circular absorbing patches of varying diameter placed at the septum and with an absorbing annular ribbon that circumscribes the entire cylinder (Figure 7A). The diameter of the circular patch (w_{pore}) and the width of the ribbon (w_{ribbon}) were varied along with the value of D_{peri} (Supporting Information Figures S8 and S9). For nonseptating cells, we used a circular patch centered at one cell tip (Figure 7A). In each simulation, the size and shape of the absorbing patch was held constant in time. To simulate fluorescence images, the particle positions were first blurred by the diffraction limit. Simulated images in space and time can then be projected onto two dimensions (as in Figure 7C, mimicking the microscopy experiments of Figures 1 and 2) or integrated over the short cell axis to produce simulated axial intensity profiles (as in Figure 7C). They can also be integrated over space to yield the time course of total GFP leakage and Δt_{GFP} (as in Figures 4 and 7B and in Table 1). For both septating and nonseptating cells, our simulations indicate that the permeable region must already be large within ~2 s and must grow even larger over the subsequent 5−10 s.

In Figure 7C, we compare the simulation results with the data from the same septating cell shown in Figure 1. The simulations match experiment best when D_{peri} is chosen in the

dx.doi.org/10.1021/bi400785j | *Biochemistry* 2013, 52, 6584−6594

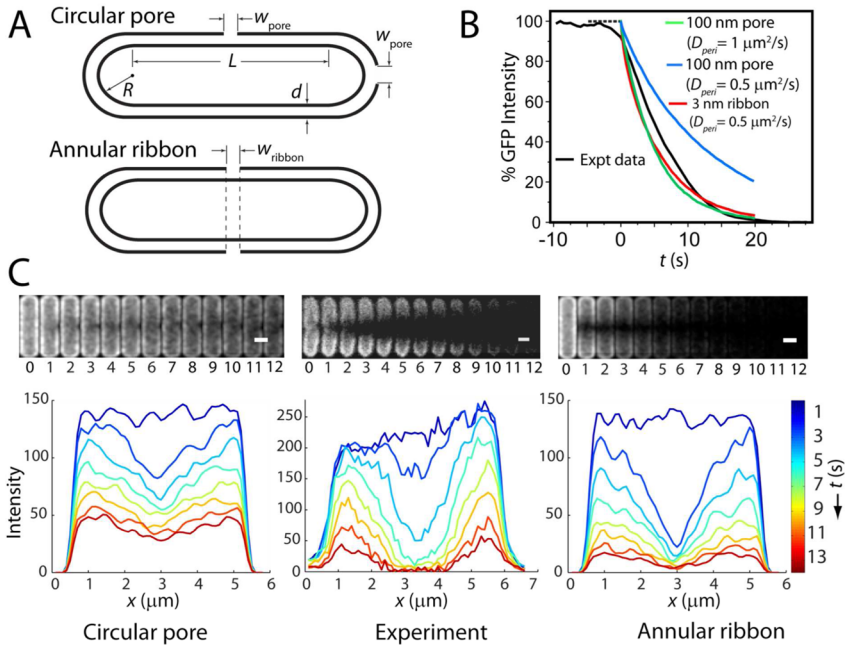

Figure 7. Monte Carlo simulations of GFP loss from periplasm. (A) Model geometry for the circular pore (both septal and end-cap) and for the annular ribbon. (B) Comparison of GFP loss from one septating cell (expt data) with different models as shown. (C) Two-dimensional experimental images and axial profiles from the same cell as in panel B (center) compared with those of the models. At left is a 100 nm pore with D_{peri} = 0.5 μm^2 s^{-1}; at right is a 3 nm annular ribbon with the same D_{peri} = 0.5 μm^2 s^{-1}. The model at left fits the data reasonably well at short times but does not decay sufficiently over 10 s. The model at right decays too fast at short times but fits the data reasonably well at longer times.

narrow range 0.5−1.0 μm^2 s^{-1}. For smaller diffusion coefficients, Δt_{GFP} becomes too long, and for larger diffusion coefficients, the observed spatial hole never becomes deep enough due to fast equilibration of the GFP distribution. Remarkably, the simulations show that in order to absorb GFP on the experimental time scale of Δt_{GFP} ∼ 10−20 s (Figure 7B), a single circular patch must have a very large diameter, ∼100−200 nm. An absorbing ribbon at the septal region also matches the time scale well with D_{peri} = 0.5 μm^2 s^{-1}, independent of the value of w_{ribbon} (Supporting Information Figure S8). Models tuned to match Δt_{GFP} decay more rapidly than in the experiment at t = 0 but less rapidly than in the experiment at later times. The model thus suggests that the OM permeability is increasing in time over the first several seconds, even in cases of nominally abrupt GFP loss curves (Figure 6).

In addition, neither a static circular patch nor a static annular ribbon mimics the time-dependent spatial distribution well (Figure 7C). The circular patch mimics the radial asymmetry at early times, but the asymmetry persists too long and the depth of the axial hole remains too shallow. The static ribbon cannot explain the radial asymmetry, but it captures the longer-term depth of the axial hole much better than the circular patch. We have not carried out simulations with time-evolving permeable patches. However, for the septating cell in Figure 1, it seems likely that the observations could be well matched by a large, localized initial patch that evolved over the first few seconds into an annular ribbon.

For nonseptating cells, the experimental results show $\langle \Delta t_{GFP} \rangle$ ∼ 10−20 s. Again, with D_{peri} = 2.0 μm^2 s^{-1} and a circular patch at the tip of the cell of diameter as large as 100−200 nm, the simulation can match the experimental GFP loss times and approximate the time-dependent GFP spatial distribution (Supporting Information Figure S10). We discuss possible interpretations of such large permeable patches below.

Simulations of Sytox Green entry into the cytoplasm would depend on the permeability of both OM and CM to Sytox Green as well as the effective binding strength of Sytox Green to DNA and its diffusion coefficient within the cytoplasm. Such a large parameter space is not well constrained by the present data. The fact that Δt_{Sytox} is consistently larger than Δt_{GFP} does not necessarily indicate that the disruptions of the cytoplasmic membrane are less permeable than those of the outer membrane. The nucleoid binding capacity is large; it may absorb a very large number of Sytox Green molecules on the way to the maximum of the green fluorescence signal.

Comparison Study of LL-37. The length and charge of LL-37 (LLGDFFRKSKEKIGKEFKRIVQRIKDFLRNLVPRTES-NH_2) and Cecropin A (KWKLFKKIEKVGQNIRDGIIKAGPAVAVVGQATQIAK-NH_2) are similar,[40] so it is of interest to compare their effects on *E. coli* in some detail. Our previous study of LL-37 focused primarily on rhodamine-labeled LL-37. Using the fast image acquisition scheme introduced here, we have studied membrane permeabilization events for unlabeled LL-37 for comparison with Cecropin A. The 12 h MIC for LL-37 is 1 μM. The timing results for permeabilization events and for the loss of GFP and the rise of Sytox Green signal are summarized in Supporting Information Table S1. As for Cecropin A, the LL-37-induced disruption of both OM and CM is localized, and there is a substantial lag time before each step. However, there are both qualitative and quantitative differences between LL-37 and Cecropin A. Like Cecropin A, LL-37 attacks septating cells earlier and disrupts the OM at the septal region, leading to complete loss of GFP. However, LL-37 then also disrupts the CM at the septal region (Supporting Information Figure S11). In contrast, Cecropin A tends to attack the CM at one end-cap.

dx.doi.org/10.1021/bi400785j | *Biochemistry* 2013, 52, 6584−6594

For nonseptating cells, LL-37 locally disrupts the OM at one end-cap (like Cecropin A) and then locally disrupts the CM *at the same end-cap*. In contrast, for Cecropin A, the location of the second event seems polarized toward the opposite end of the cell (Figure 3). These differences in mode of attack are illustrated in Figure 8 for a typical nonseptating case and in Supporting Information Figure S11 for a typical sepatating example.

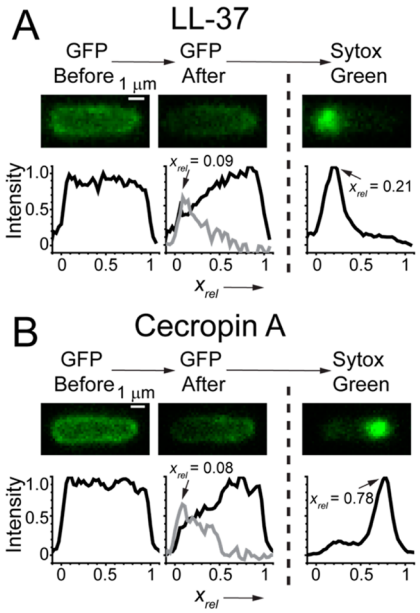

Figure 8. Comparison of the typical attack mode of (A) LL-37 and (B) Cecropin A on nonseptating cells. Both attack the OM at one end-cap; LL-37 attacks the CM at the *same* end-cap, but Cecropin A attacks the CM at the *opposite* end-cap. For (A) and (B), the two images and axial linescans at left were obtained just before and just after OM permeabilization to GFP. Subtraction of the two linescans makes the gray difference plot whose maximum determines x_{rel} for the OM permeabilization event. The image and linescan at right shows the initial localized Sytox Green signal. We determine x_{rel} for CM permeabilization from the peak position of the axial linescan. See also Supporting Information (Figure S2).

Comparisons of timing events between LL-37 and Cecropin A should be made with caution. The most appropriate comparison would be carried out at equal adsorbed surface concentration of the two peptides. However, in this work with unlabeled peptides, we can only compare the action of the two peptides at equivalent bulk concentrations relative to the MIC. Bulk peptide concentrations are only nominal due to unquantifiable losses of AMP at the surfaces of the chamber. Nevertheless, LL-37 at nominal bulk concentration of 4 μM (four times the MIC) takes much longer to disrupt the OM than Cecropin A at nominal bulk concentration of 2 μM (again four times the MIC). For all cells combined, $\langle t_{OM} \rangle$ = 670 ± 540 s for LL-37 and 180 ± 100 s for Cecropin A. The same holds for the lag time between disruption of the OM to GFP and disruption of the CM to Sytox Green ($\langle t_{CM} - t_{OM} \rangle$ = 320 ± 280 s for LL-37 and 39 ± 17 s for Cecropin A). Surprisingly, although LL-37 preferentially attacks septating cells first, the time lag $\langle t_{CM} - t_{OM} \rangle$ is 4-fold *longer* for septating cells than for nonseptating cells.

Alternatively, we can compare LL-37 at 8 μM with Cecropin A at 2 μM so that the lag times $\langle t_{OM} \rangle$ become comparable for the two AMPs (220 ± 170 s vs 180 ± 100 s). Averaged over all cells, the second lag time $\langle t_{CM} - t_{OM} \rangle$ remains substantially longer for LL-37 (130 ± 150 s vs 39 ± 17 s), and again, the difference is dominated by the long lag times for LL-37 to disrupt the CM of septating cells. Perhaps LL-37 binds to elements within the periplasm more strongly than Cecropin A and is thus less available for attack on the CM.

As evidenced by Δt_{GFP}, the degree of OM permeability induced by LL-37 is smaller than that produced by Cecropin A. Again comparing 8 μM LL-37 with 2 μM Cecropin A (to make $\langle t_{OM} \rangle$ comparable), $\langle \Delta t_{GFP} \rangle$ over all cells is 60 ± 64 s for LL-37 vs 15 ± 10 s for Cecropin A, a factor of 4 slower. Comparing 4 μM LL-37 with 1 μM Cecropin A, GFP loss is a factor of 6 slower for LL-37. In contrast, $\langle \Delta t_{Sytox} \rangle$ is comparable for LL-37 and Cecropin A.

In summary, at comparable concentrations relative to the MIC, LL-37 permeabilizes the OM and CM much slower than Cecropin A. In salty solution-like growth medium, LL-37 folds into helical bundles and forms oligomers,[41] whereas Cecropin A exists primarily as monomers.[26] The slow kinetics of the LL-37 mediated attack on *E. coli* could be related to the stability of oligomeric bundles within the lipopolysaccharide layer.

DISCUSSION

Localized, Persistent Membrane Disruption Events. For the action of Cecropin A on both the outer and cytoplasmic membranes of *E. coli*, we find clear evidence of *localized* membrane disruption events *that persist and are stable in time*. In some studies of content release from LUVs, membrane disruptions evidently heal over time (graded release kinetics).[2,27] This may be due to the ability of the LUV to equilibrate the AMP concentration and relieve differential surface pressure across the two leaflets before all content is released. However, experiments on single GUVs have not revealed membrane disruptions that heal over time.[7−11] Such a healing mechanism is presumably not available for the OM of *E. coli*. Cecropin A molecules that translocate into the periplasm may bind to periplasmic components such as the peptidoglycan layer or to the outer leaflet of the cytoplasmic membrane, thus maintaining differential AMP concentration between the outer and inner leaflets of the OM.

Localized permeabilization of the OM of *E. coli* by Cecropin A is inferred from the initial radial asymmetry of the dark patch that gradually symmetrizes and spreads axially as well (Figure 1). Comparison of the time evolution of the shape of the axial intensity distribution with Monte Carlo simulations indicates that the permeability of the membrane disruption gradually increases over several seconds (Figure 7B,C). Complete leakage of the periplasmic GFP to the surrounding medium and subsequent entry of Sytox Green across the OM demonstrates that the OM disruption remains for at least several minutes.

For the cytoplasmic membrane, localized disruption is inferred from the small initial spot of Sytox Green fluorescence, which then slowly spreads across the nucleoids. The CM remains permeable to Sytox Green for at least ~2 min, the time scale of Sytox Green staining of the nucleoid, and probably for much longer. The earliest discernible images of Sytox Green are not diffraction limited. For Cecropin A and LL-37 on *E. coli*, we estimate the initial full width at half-maximum intensity (FWHM) to be 330−440 nm, significantly larger than the diffraction limit of 200 nm FWHM at the emission wavelength of 540 nm. The same was true for LL-37 on *B. subtilis*.[34] The breadth of the initial Sytox Green spots may be due in part to

dx.doi.org/10.1021/bi400785j | *Biochemistry* 2013, 52, 6584−6594

the breadth of the initial membrane disruption, consistent with the inferences from the Monte Carlo simulations. However, the structure of the cytoplasm also plays a role. Under these growth conditions, *E. coli* shows strong segregation of the two nucleoid lobes from three interspersed ribosome-rich regions (cell center and two end-caps).[42] When Sytox Green enters the cytoplasm at either the septal region or an end-cap, it must first diffuse through a ribosome-rich region before encountering dense DNA. Some spreading during this transit will inevitably occur.

Our data do not enable us to classify the observed membrane disruptions as pores or carpets. Neither our observations nor the Monte Carlo models can distinguish a well-defined pore[14] from a chaotic pore[19] from a localized "carpet patch"[21] from a leaky hexagonal phase analogue.[22] The simulations of GFP efflux from the periplasmic space demonstrate that within a few seconds, the outer membrane acquires permeability comparable to that of a single pore of ∼100 nm diameter. A toroidal pore can in principle expand to any size; in fact, micrometer-sized, AMP-induced pores were recently observed by AFM in a planar lipid bilayer.[43] However, we expect that rapid formation of such a large pore in the OM would lead to blebbing of the cytoplasm, which is not observed. The GFP loss data are equally consistent with the abrupt formation of *many* smaller pores in a ∼100 nm diameter region of space. As is well-known in the theory of diffusion to absorbing patches,[39] a sparse set of small absorbers will capture molecules almost as rapidly as a completely absorbing patch covering the same area. In a pore-like model, the increasing OM permeability over several seconds inferred from comparisons with the Monte Carlo simulations would be due to a rapid increase in the number of pores and perhaps, also, in the area they cover. The permeable region may evolve from a localized patch to a ribbon surrounding the septal region, as suggested in the examples in Figures 1 and 7B,C. The GFP release data are also consistent with formation of a localized, highly permeable "carpet patch" of at least 100 nm diameter that subsequently spreads.

Formation of the initial membrane disruption takes minutes, but the subsequent enhancement of the permeability occurs over only a few seconds. This suggests that successful nucleation of the initial localized permeabilization site lowers the free energy barrier to formation of a larger permeabilization region, a kind of "cooperativity of permeabilization".

Preferential Attack at Curved Membrane Surfaces. Both Cecropin A and LL-37 attack septating cells earlier than nonseptating cells. For septating cells, both AMPs always permeabilize the OM in the septal region. This is the region of active biosynthesis of the curved cell wall, including the lipopolysaccharide layer, underlying membrane, and the peptidoglycan layer. For nonseptating cells, both Cecropin A and LL-37 permeabilize the OM at one end-cap, where no cell wall synthesis is occurring. Intriguingly, in the five cells observed for sufficient time, Cecropin A permeabilizes the *new* pole (the site of the most recent septation) of nonseptating cells in preference to the old pole. The septal region of septating cells and the new pole of nonseptating cells both contain elements of the divisome machinery. Labeling studies have shown that in newborn cells, the poles and division septum are enriched in anionic phospholipids such as cardiolipin.[44] The septal region is also the site of initiation of DNA replication by DnaA.[45] It is possible that a cardiolipin-rich domain at the septum recruits the DNA replication machinery, and subsequently, the early cell division proteins such as FtsZ, FtsA, and ZipA.[46] Following cell division, cardiolipin might persist at the new pole before eventually migrating to the next division site. Cardiolipin is known to be present on the outer leaflet of the OM. Our data suggest that the special composition of the curved outer membrane at a septum or a new pole somehow facilitates permeabilization by Cecropin A. In a pore model of membrane disruption, the positively curved cardiolipin might alleviate strain at the curved edge of a toroidal pore.[47] It might also be useful in nucleating a highly curved hexagonal-like phase.

The axial distribution of OM and CM permeabilization events is quite different for LL-37 and Cecropin A (Figure 8 and Supporting Information Figure S11). Evidently, peptide sequence strongly affects the point of attack. For septating cells, LL-37 typically permeabilizes the CM at the septal region, the same location as the OM permeabilization. For nonseptating cells, LL-37 permeabilizes both the OM and CM near the same end-cap. In contrast, Cecropin A permeabilizes the CM far from the initial entry point into the periplasm (Figures 3 and 8 and Supporting Information Figure S11). The explanation is not obvious. Although the length and net charge of the two peptides are similar, the distribution of charges along the sequence is quite different. In LL-37, positive and negative charges are widely distributed, whereas in Cecropin A, the helix nearest to the N-terminus (residues 8−21) contains most of the charges and the other helix (residues 25−37) is mainly hydrophobic.

Kinetics of Membrane Disruption. This study of unlabeled Cecropin A lacks key ingredients necessary to build a quantitative kinetics model of membrane disruption, so the discussion that follows is necessarily speculative. Without flowing Cecropin A through the observation chamber, the bulk concentration remains ill-defined. More importantly, we lack information about the time-dependent concentration of Cecropin A *at the cell surface,* within the lipopolysaccharide (LPS)/outer membrane layer. Finally, we do not know the diffusion coefficient of Cecropin A within the LPS layer.

Nevertheless, the present results allow us to infer several qualitative features of the membrane disruption mechanism. Disruption of the OM by Cecropin A is a rare event that occurs only after a mean lag time of 2−9 min. A possibly analogous lag time has been observed in kinetics measurements of the disruption of GUVs by various AMPs.[10,11,16] Above a threshold bulk Cecropin A concentration, the mean lag time $\langle t_{OM} \rangle$ to OM permeabilization decreases with increasing bulk concentration, but only roughly linearly (Table 1). The mean lag time $\langle (t_{OM} - t_{CM}) \rangle$ between OM permeabilization and CM permeabilization is also weakly dependent on bulk Cecropin A concentration and shows no threshold. This suggests that any Cecropin A concentration sufficiently high to permeabilize the OM quickly creates a periplasmic Cecropin A concentration that lies well above the threshold for permeabilization of the CM.

The long lag time to OM permeabilization might arise from slow uptake of AMPs by the LPS layer. However, our earlier study of rhodamine-labeled LL-37[33] and unpublished data on rhodamine-labeled Cecropin A indicate that for both septating and nonseptating cells the AMP equilibrates between the lipopolysaccharide layer (LPS) and the bulk in less than 1 min. Disruption of the OM typically occurs only after a much longer lag time. Evidently, the lag time to OM permeabilization is not primarily due to slow accumulation of Cecropin A within the LPS layer. Alternatively, slow diffusion within the LPS layer might severely limit the ability of Cecropin A to reach the membrane and disrupt it. Future studies using fluorescently

labeled Cecropin A will provide quantitative data on the rate of equilibration of the bulk and surface-bound populations and also the diffusion constant of Cecropin A within the LPS layer.

The long lag times to OM and CM permeabilization combined with the existence of a threshold concentration for OM permeabilization suggest that membrane disruption involves a nucleation step that is rare and difficult due to a large free energy barrier. Suppose nucleation of a pore-like structure involved cooperative, simultaneous insertion of *multiple* Cecropin A monomers into the bilayer. Then classical nucleation theory predicts that the mean lag time to formation of a multipeptide disruption from monomers scales as $[M]^n$, where $[M]$ is the surface concentration of monomer and n is the number of monomers in the critical nucleus configuration.[48] Still, the observed mean lag time to OM permeabilization decreases only roughly linearly with *bulk* Cecropin A concentration, not as some higher power as suggested by nucleation theory. A remarkably similar combination of observations was made for Bax-mediated pore formation in isolated mitochondrial outer membranes.[49] The lag time to membrane disruption was highly variable, but the mean rate of pore formation depended only linearly on the Bax concentration.

It is possible that for Cecropin A, the threshold surface concentration for pore formation in the OM is not much smaller than the saturation limit for binding of peptide to the LPS layer. If so, then the equilibrium surface concentration would change only slowly with bulk concentration in the regime that induces pores. The critical number n could still be substantial, and nucleation theory could still hold. Future measurement of lag time distributions vs *surface* Cecropin A concentration using labeled peptide are an important next step. If a linear dependence of mean lag time on surface concentration is observed, it may prove useful to consider "lipocentric" models of pore formation, in which the peptide serves as a kind of catalyst that induces tension within the bilayer and then stabilizes the resulting transient pores.[50]

■ ASSOCIATED CONTENT

Supporting Information

(1) Explanation of how axial and transverse intensity profiles are created. (2) Definition of the relative axial coordinate system x_{rel} and explanation of how we estimate the axial positions at which the OM is permeabilized to GFP and the CM is permeabilized to Sytox Green. (3) Additional histograms of the timing and duration of permeabilization events at nominal 1 and 2 μM bulk Cecropin A concentration. (4) Figure S6 showing the subtle slowing of growth rate immediately after the Cecropin A addition. (5) Further details of how the Monte Carlo simulations are carried out, plus figures showing one model trajectory and how the model outcomes depend on input parameters. (6) Comparison of the attack of Cecropin A and LL-37 on a septating cell. (7) Table S1, describing timing and duration of permeabilization events for LL-37 attacking *E. coli*. (8) A movie showing the attack of Cecropin A on one septating cell and one nonseptating cell. This material is available free of charge via the Internet at http://pubs.acs.org.

■ AUTHOR INFORMATION

Corresponding Author

*J. C. Weisshaar. Phone: 608 262 0266. E-mail: weisshaar@chem.wisc.edu.

Funding

Research reported in this publication was supported by the National Institute of General Medical Sciences of the National Institutes of Health under Award Number R01GM094510. The content is solely the responsibility of the authors and does not necessarily represent the official views of the National Institutes of Health.

Notes

The authors declare no competing financial interest.

■ ACKNOWLEDGMENTS

A helpful discussion with Prof. Qiang Cui is gratefully acknowledged.

■ ABBREVIATIONS

AMP, antimicrobial peptide; OM, outer membrane; CM, cytoplasmic membrane; GUV, giant unilamellar vesicle; LUV, large unilamellar vesicle; MIC, minimum inhibitory concentration; GFP, green fluorescent protein; ROI, region of interest

■ REFERENCES

(1) Wang, Z., and Wang, G. (2004) APD: the Antimicrobial Peptide Database. *Nucleic Acids Res. 32*, D590−592.

(2) Wimley, W. C., and Hristova, K. (2011) Antimicrobial peptides: successes, challenges and unanswered questions. *J. Membr. Biol. 239*, 27−34.

(3) Brogden, K. A. (2005) Antimicrobial peptides: pore formers or metabolic inhibitors in bacteria? *Nat. Rev. Microbiol. 3*, 238−250.

(4) Mowery, B. P., Lindner, A. H., Weisblum, B., Stahl, S. S., and Gellman, S. H. (2009) Structure-activity relationships among random nylon-3 copolymers that mimic antibacterial host-defense peptides. *J. Am. Chem. Soc. 131*, 9735−9745.

(5) Clark, K. S., Svetlovics, J., McKeown, A. N., Huskins, L., and Almeida, P. F. (2011) What determines the activity of antimicrobial and cytolytic peptides in model membranes. *Biochemistry 50*, 7919−7932.

(6) Almeida, P. F., and Pokorny, A. (2009) Mechanisms of antimicrobial, cytolytic, and cell-penetrating peptides: from kinetics to thermodynamics. *Biochemistry 48*, 8083−8093.

(7) Hung, W. C., Chen, F. Y., Lee, C. C., Sun, Y., Lee, M. T., and Huang, H. W. (2008) Membrane-thinning effect of curcumin. *Biophys. J. 94*, 4331−4338.

(8) Huang, H. W. (2006) Molecular mechanism of antimicrobial peptides: the origin of cooperativity. *Biochim. Biophys. Acta 1758*, 1292−1302.

(9) Huang, H. W., Chen, F. Y., and Lee, M. T. (2004) Molecular mechanism of Peptide-induced pores in membranes. *Phys. Rev. Lett. 92*, 198304.

(10) Tamba, Y., Ohba, S., Kubota, M., Yoshioka, H., Yoshioka, H., and Yamazaki, M. (2007) Single GUV method reveals interaction of tea catechin (-)-epigallocatechin gallate with lipid membranes. *Biophys. J. 92*, 3178−3194.

(11) Tamba, Y., and Yamazaki, M. (2005) Single giant unilamellar vesicle method reveals effect of antimicrobial peptide magainin 2 on membrane permeability. *Biochemistry 44*, 15823−15833.

(12) Wimley, W. C. (2010) Describing the mechanism of antimicrobial peptide action with the interfacial activity model. *ACS Chem. Biol. 5*, 905−917.

(13) Qian, S., Wang, W., Yang, L., and Huang, H. W. (2008) Structure of the alamethicin pore reconstructed by x-ray diffraction analysis. *Biophys. J. 94*, 3512−3522.

(14) Lee, C. C., Sun, Y., Qian, S., and Huang, H. W. (2011) Transmembrane pores formed by human antimicrobial peptide LL-37. *Biophys. J. 100*, 1688−1696.

(15) Lee, E., Jeong, K. W., Lee, J., Shin, A., Kim, J. K., Lee, J., Lee, D. G., and Kim, Y. (2013) Structure-activity relationships of cecropin-like

peptides and their interactions with phospholipid membrane. *BMB Rep. 46*, 282−287.
(16) Lee, M. T., Hung, W. C., Chen, F. Y., and Huang, H. W. (2008) Mechanism and kinetics of pore formation in membranes by water-soluble amphipathic peptides. *Proc. Natl. Acad. Sci. U. S. A. 105*, 5087−5092.
(17) Schlamadinger, D. E., Wang, Y., McCammon, J. A., and Kim, J. E. (2012) Spectroscopic and computational study of melittin, cecropin A, and the hybrid peptide CM15. *J. Phys. Chem. B 116*, 10600−10608.
(18) Leontiadou, H., Mark, A. E., and Marrink, S. J. (2006) Antimicrobial peptides in action. *J. Am. Chem. Soc. 128*, 12156−12161.
(19) Axelsen, P. H. (2008) A chaotic pore model of polypeptide antibiotic action. *Biophys. J. 94*, 1549−1550.
(20) Shai, Y. (2002) Mode of action of membrane active antimicrobial peptides. *Biopolymers 66*, 236−248.
(21) Shai, Y. (1999) Mechanism of the binding, insertion and destabilization of phospholipid bilayer membranes by alpha-helical antimicrobial and cell non-selective membrane-lytic peptides. *Biochim. Biophys. Acta 1462*, 55−70.
(22) Schmidt, N. W., Tai, K. P., Kamdar, K., Mishra, A., Lai, G. H., Zhao, K., Ouellette, A. J., and Wong, G. C. (2012) Arginine in alpha-defensins: differential effects on bactericidal activity correspond to geometry of membrane curvature generation and peptide-lipid phase behavior. *J. Biol. Chem. 287*, 21866−21872.
(23) Yang, L., Gordon, V. D., Mishra, A., Som, A., Purdy, K. R., Davis, M. A., Tew, G. N., and Wong, G. C. (2007) Synthetic antimicrobial oligomers induce a composition-dependent topological transition in membranes. *J. Am. Chem. Soc. 129*, 12141−12147.
(24) Steiner, H., Hultmark, D., Engstrom, A., Bennich, H., and Boman, H. G. (1981) Sequence and specificity of two antibacterial proteins involved in insect immunity. *Nature 292*, 246−248.
(25) Marassi, F. M., Opella, S. J., Juvvadi, P., and Merrifield, R. B. (1999) Orientation of cecropin A helices in phospholipid bilayers determined by solid-state NMR spectroscopy. *Biophys. J. 77*, 3152−3155.
(26) Silvestro, L., and Axelsen, P. H. (2000) Membrane-induced folding of cecropin A. *Biophys. J. 79*, 1465−1477.
(27) Gregory, S. M., Cavenaugh, A., Journigan, V., Pokorny, A., and Almeida, P. F. (2008) A quantitative model for the all-or-none permeabilization of phospholipid vesicles by the antimicrobial peptide cecropin A. *Biophys. J. 94*, 1667−1680.
(28) Wade, D., Boman, A., Wahlin, B., Drain, C. M., Andreu, D., Boman, H. G., and Merrifield, R. B. (1990) All-D amino acid-containing channel-forming antibiotic peptides. *Proc. Natl. Acad. Sci. U. S. A. 87*, 4761−4765.
(29) Steiner, H., Andreu, D., and Merrifield, R. B. (1988) Binding and action of cecropin and cecropin analogues: antibacterial peptides from insects. *Biochim. Biophys. Acta 939*, 260−266.
(30) Christensen, B., Fink, J., Merrifield, R. B., and Mauzerall, D. (1988) Channel-forming properties of cecropins and related model compounds incorporated into planar lipid membranes. *Proc. Natl. Acad. Sci. U. S. A. 85*, 5072−5076.
(31) Silvestro, L., Gupta, K., Weiser, J. N., and Axelsen, P. H. (1997) The concentration-dependent membrane activity of cecropin A. *Biochemistry 36*, 11452−11460.
(32) Silvestro, L., Weiser, J. N., and Axelsen, P. H. (2000) Antibacterial and antimembrane activities of cecropin A in Escherichia coli. *Antimicrob. Agents Chemother. 44*, 602−607.
(33) Sochacki, K. A., Barns, K. J., Bucki, R., and Weisshaar, J. C. (2011) Real-time attack on single Escherichia coli cells by the human antimicrobial peptide LL-37. *Proc. Natl. Acad. Sci. U. S. A. 108*, E77−81.
(34) Barns, K. J., and Weisshaar, J. C. (2013) Real-time attack of LL-37 on single Bacillus subtilis cells. *Biochim. Biophys. Acta 1828*, 1511−1520.
(35) Neidhardt, F. C., Bloch, P. L., and Smith, D. F. (1974) Culture medium for enterobacteria. *J. Bacteriol. 119*, 736−747.
(36) Sochacki, K. A., Shkel, I. A., Record, M. T., and Weisshaar, J. C. (2011) Protein diffusion in the periplasm of E. coli under osmotic stress. *Biophys. J. 100*, 22−31.
(37) Sargent, F. (2007) The twin-arginine transport system: moving folded proteins across membranes. *Biochem. Soc. Trans. 35*, 835−847.
(38) Hong, R. W., Shchepetov, M., Weiser, J. N., and Axelsen, P. H. (2003) Transcriptional profile of the Escherichia coli response to the antimicrobial insect peptide cecropin A. *Antimicrob. Agents Chemother. 47*, 1−6.
(39) Berg, H. C. (1993) *Random Walks in Biology*, Princeton University Books, Princeton, NJ.
(40) Porcelli, F., Verardi, R., Shi, L., Henzler-Wildman, K. A., Ramamoorthy, A., and Veglia, G. (2008) NMR structure of the cathelicidin-derived human antimicrobial peptide LL-37 in dodecylphosphocholine micelles. *Biochemistry 47*, 5565−5572.
(41) Oren, Z., Lerman, J. C., Gudmundsson, G. H., Agerberth, B., and Shai, Y. (1999) Structure and organization of the human antimicrobial peptide LL-37 in phospholipid membranes: relevance to the molecular basis for its non-cell-selective activity. *Biochem. J. 341* (Pt 3), 501−513.
(42) Bakshi, S., Siryaporn, A., Goulian, M., and Weisshaar, J. C. (2012) Superresolution imaging of ribosomes and RNA polymerase in live Escherichia coli cells. *Mol. Microbiol. 85*, 21−38.
(43) Rakowska, P. D., Jiang, H., Ray, S., Pyne, A., Lamarre, B., Carr, M., Judge, P. J., Ravi, J., Gerling, U. I. M., Koksch, B., Martyna, G. J., Hoogenboom, B. W., Watts, A., Crain, J., Grovenor, C. R., and Ryadnov, M. G. (2013) Nanoscale imaging reveals laterally expanding antimicrobial pores in lipid bilayers. *Proc. Natl. Acad. Sci. U. S. A. 110*, 8918−8923.
(44) Mileykovskaya, E., and Dowhan, W. (2009) Cardiolipin membrane domains in prokaryotes and eukaryotes. *Biochim. Biophys. Acta 1788*, 2084−2091.
(45) Pogliano, K., Pogliano, J., and Becker, E. (2003) Chromosome segregation in Eubacteria. *Curr. Opin. Microbiol. 6*, 586−593.
(46) Lutkenhaus, J., Pichoff, S., and Du, S. (2012) Bacterial cytokinesis: From Z ring to divisome. *Cytoskeleton 69*, 778−790.
(47) Lee, M. T., Hung, W. C., Chen, F. Y., and Huang, H. W. (2005) Many-body effect of antimicrobial peptides: on the correlation between lipid's spontaneous curvature and pore formation. *Biophys. J. 89*, 4006−4016.
(48) Powers, E. T., and Powers, D. L. (2006) The kinetics of nucleated polymerizations at high concentrations: amyloid fibril formation near and above the "supercritical concentration". *Biophys. J. 91*, 122−132.
(49) Kushnareva, Y., Andreyev, A. Y., Kuwana, T., and Newmeyer, D. D. (2012) Bax activation initiates the assembly of a multimeric catalyst that facilitates Bax pore formation in mitochondrial outer membranes. *PLoS Biol. 10*, e1001394.
(50) Fuertes, G., Gimenez, D., Esteban-Martin, S., Sanchez-Munoz, O. L., and Salgado, J. (2011) A lipocentric view of peptide-induced pores. *Eur. Biophys. J. 40*, 399−415.